K-SCATTERING IN DEUTERIUM
100 TO 250 MEV/C

VINCENT J. MANARA, JR.

UCRL-8772
Physics and Mathematics

UNIVERSITY OF CALIFORNIA

Lawrence Radiation Laboratory
Berkeley, California

Contract No. W-7405-eng-48

K^- SCATTERING IN DEUTERIUM AT 100 to 250 Mev/c

Vincent J. Manara Jr.

May 25, 1959

Submitted in partial fulfillment
of the requirements for the degree of

MASTER OF SCIENCE
IN
PHYSICS

United States Naval Postgraduate School
Monterey, California

Printed for the U. S. Atomic Energy Commission

Printed in USA. Price $1.50. Available from the
Office of Technical Services
U.S. Department of Commerce
Washington 25, D. C.

K^- SCATTERING IN DEUTERIUM AT 100 to 250 Mev/c

Contents

K^- SCATTERING IN DEUTERIUM AT 100 to 250 Mev/c

Vincent J. Manara Jr.

Lawrence Radiation Laboratory
University of California
Berkeley, California

May 25, 1959

ABSTRACT

An investigation of K^--meson elastic and inelastic scattering at 100 to 250 Mev/c is reported. Experimentally determined cross sections were compared to theoretical cross sections from the two Dalitz phase-shift solutions for K^--p scattering. Within statistical accuracy, the second Dalitz solution is found to be correct.

K^- SCATTERING IN DEUTERIUM AT 100 to 250 Mev/c

Vincent J. Manara Jr.

Lawrence Radiation Laboratory
University of California
Berkeley, California

May 25, 1959

INTRODUCTION

For several years the Alvarez group has been engaged in the study of interactions between low-energy K^- mesons and protons. In order to extend this investigation, the Lawrence Radiation Laboratory bubble chamber was filled with deuterium and exposed to low-energy K^- mesons produced in the Bevatron. The experiment was designed to

(a) check the branching rules for hyperon production deduced from the principle of charge independence in strange-particle interactions, [1]

(b) investigate the scattering of low-energy K^- mesons from deuterons.

Dalitz has performed a comprehensive analysis of the low energy K^- meson -proton interactions in terms of a short range S-wave interaction . [2] Because of statistical limitations in the experimental data, there are ambiguities in the solutions. The main purpose of this investigation is to try to use the scatterings that occur in deuterium in order to determine the nature of the correct solution. By use of a simple model of the deuteron, the scattering cross sections may be estimated from a knowledge of the elementary K^- meson–nucleon scattering amplitudes. We are led to two distinct predictions for the K^- meson—deuterium cross sections, one of which should agree with the experimental data.

As a by-product of this investigation, we shall be able to perform a separation of the real scattering events from events involving hyperon

production but looking superficially like scatterings. This separation is necessary so that a meaningful comparison may be made between the experimental hyperon branching ratios and those deduced from the principle of charge independence in strange-particle interactions.

EXPERIMENTAL APPARATUS

A 450-Mev/c K^--meson beam was obtained from the Bevatron through the use of a target and spectrometer system reported by Horwitz et al. (Fig. 1).[3] After emerging from the coaxial electromagnetic spectrometer the K^- mesons were slowed down by a suitable absorber so that approximately 75% came to rest in the 15-inch Lawrence Radiation Laboratory deuterium bubble chamber (Fig. 2). The resulting incident beam contained one K^- meson per 1000 background tracks.

Four stereo views of each expansion were taken on 35 mm film by cameras positioned above the chamber. After a scanning and identification of events, measurements were carried out with the UCRL precision track-measuring machine (Franckenstein). This device semiautomatically punches onto IBM cards the pertinent coordinates of tracks undergoing measurement. All further computations are then performed with the aid of an IBM 650 digital computer.

ANALYSIS OF DATA

General Analysis Techniques

Approximately 46,500 photographs were taken during the run. These were "pick-tooth" scanned by trained technicians. In this method, the scanner is limited, by means of a small mask on the film retainer of the scanning projector, to examination of the upstream 10 cm of the entering beam. By looking only for incoming negative heavily ionizing tracks, the scanner obtains a sample of events independent of the nature of the final interaction. Proper normalization then allows calculation of branching ratios and interaction cross sections free of scanning biases.

Of the 3300 K^- mesons that entered the chamber, 2200 interacted to produce hyperons and 450 decayed. The remainder did not interact and had sufficient momentum to pass through the chamber. Using the scanners' records, a physicist verified the nature of each interaction. Useful events were then sketched and measured on the Franckenstein.

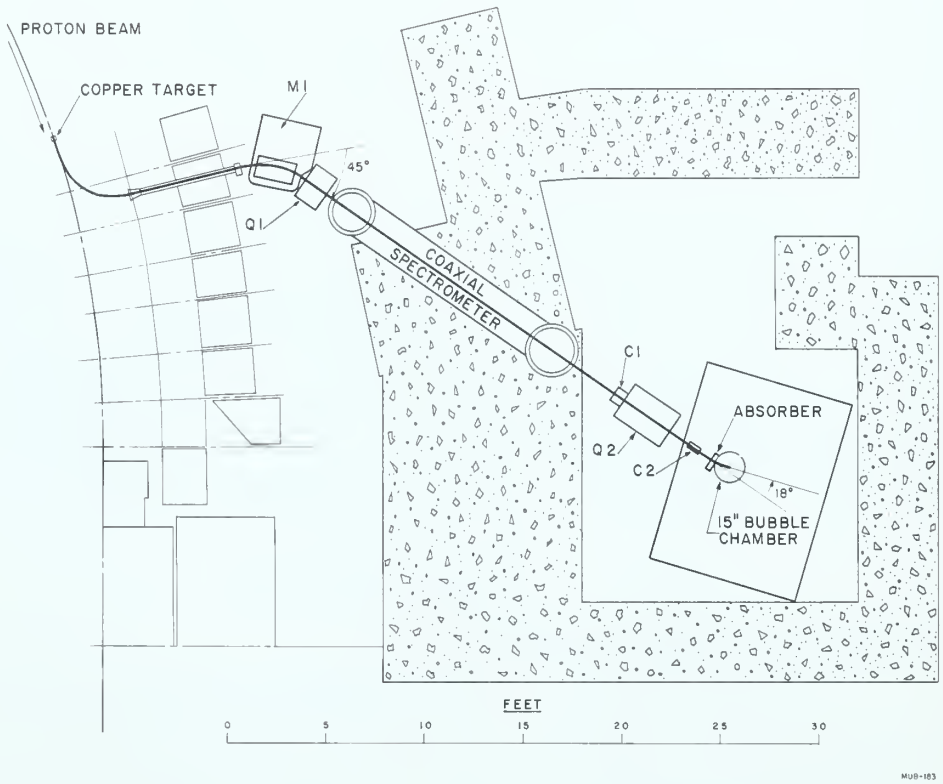

Fig. 1. Target and spectrometer system.

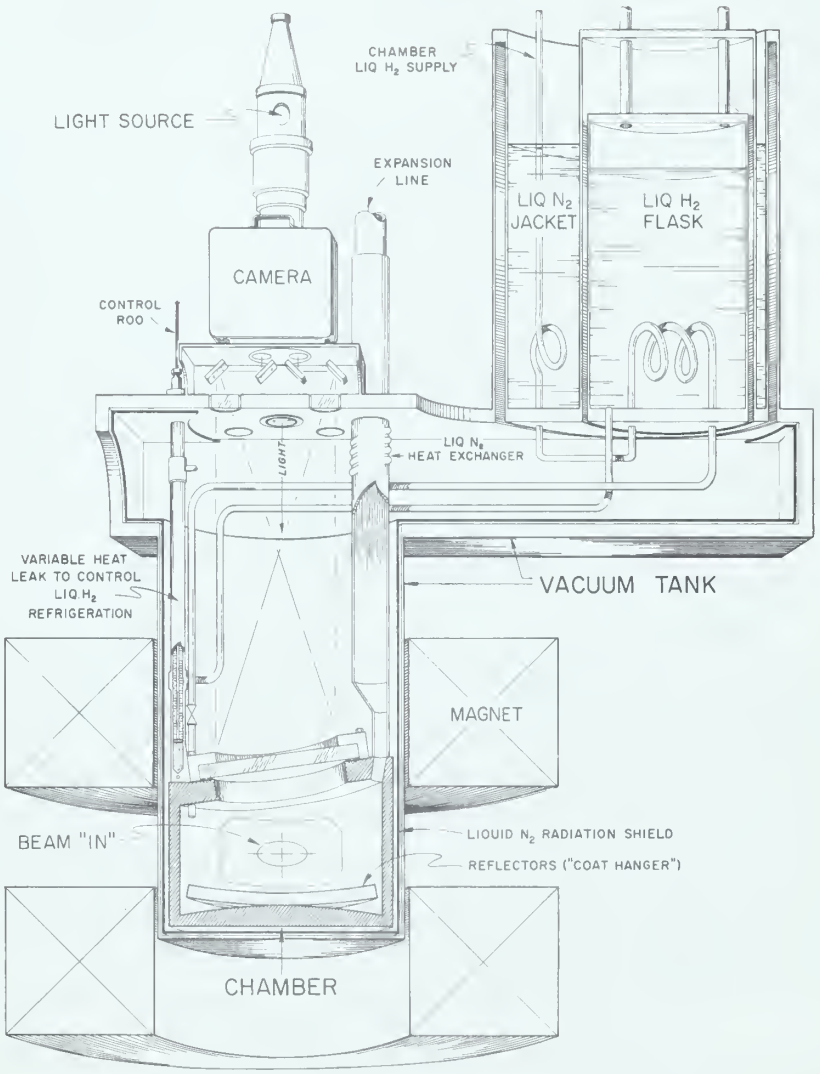

Fig. 2. Lawrence Radiation Laboratory 15-inch deuterium bubble chamber.

Selection of Events

In order to eliminate biases in the selection of events, it was necessary to limit acceptable events to a volume of the chamber, the "fiducial volume" (defined with respect to the fiducial marks), satisfying the following criteria:

(a) Since a good measurement of the momentum of the incident K^- meson was critical, the distance between the point at which the meson became illuminated and the point at which it entered the fiducial volume must be greater than 6 cm.

(b) Because of the inhomogeneity of illumination near the edge of the chamber, the fiducial volume must be confined to a distance greater than 5 cm from the edges.

(c) The fiducial volume must be greater than 5 cm from the top or bottom of the chamber so that hyperons produced in interactions decay within the visible volume of the chamber.

It was found possible to select a satisfactory volume which was still large enough so that 75% of all interactions occurred within it. The lateral extent of this fiducial volume was defined by a template which could be used on the scanning projector so that events lying outside this volume could be immediately rejected. The final selection of events was made by an IBM 650 program which examined the coordinates of the interaction vertex with respect to fiducial marks on the glass window of the bubble chamber.

Kinematic Analysis of Scatterings

Each event was treated first as an elastic scattering. For the cases in which the K^- meson and the recoil deuteron came to rest in the chamber, the momentum (magnitude and angle) of the scattered K^- meson in the laboratory system were taken as known quantities. An IBM 650 program computed

(a) the momenta of the incident K^- meson and the recoil deuteron,

(b) the angle between the incident K^- meson and the recoil deuteron,

(c) the angle of scattering in the center-of-mass system.

Both measured and computed values were included in the output of this program. (See Appendix I.)

For a second analysis, each event was treated as an inelastic scattering. The vector momenta of the scattered K^- meson and the recoil particle (now assumed a proton) were used as input data. The program computed

(a) the momentum of the incident K^-,

(b) the momentum of the recoil neutron,

(c) the azimuthal and dip angles of the scattered K^- in a new coordinate system,

(d) the azimuthal and dip angles of the recoil proton and neutron in this new coordinate system,

(e) the azimuthal and dip angles of the neutron in the laboratory system.

(See Appendix II for discussion of problem.)

The momentum transfer to the deuteron for an elastic scattering was computed for each event.

Classification of Events

When K^- mesons interact in deuterium, many possible interactions may occur. Because the strangeness quantum number associated with K^- mesons (-1) must be conserved, all absorptions lead to the production of hyperons. The most important reactions are:

$$K^- + D \rightarrow \Sigma^+ + \pi^- + n \quad (1)$$
$$K^- + D \rightarrow \Sigma^- + \pi^+ + n \quad (2)$$
$$K^- + D \rightarrow \Sigma^0 + \pi^0 + n \quad (3)$$
$$K^- + D \rightarrow \Sigma^- + \pi^0 + p \quad (4)$$
$$K^- + D \rightarrow \Sigma^0 + \pi^- + p \quad (5)$$
$$K^- + D \rightarrow \Lambda + \pi^0 + n \quad (6)$$
$$K^- + D \rightarrow \Lambda + \pi^- + p \quad (7)$$

In addition, the K^- meson may decay in flight,

$$K^- \rightarrow \pi^- + \pi^0$$
$$K^- \rightarrow \mu^- + \nu \quad (8)$$
$$K^- \rightarrow \mu^- + \pi^0 + \nu,$$

or simply scatter from a deuteron before undergoing an interaction,

$$K^- + d \rightarrow K^- + d \text{ (elastic)}, \quad (9)$$
$$K^- + p + n \text{ (inelastic)}. \quad (10)$$

We are concerned with the reactions (9) and (10) in this work. Unfortunately, many of the reactions (1) through (8) have the same appearance in the bubble chamber, and frequently it is possible to assign only a most probable interpretation to a given event.

Before a detailed kinematic analysis was attempted all events relevant to this study were separated into two groups:

1. Definite scatterings (Fig. 3)
   (a) All interactions followed by the production of a definitely identified hyperon (we thus know that a K^- meson left the first vertex).
   (b) All interactions for which the length of the emergent particle was greater than 2.5 cm. (This ensured that reactions of Type (4) were not included, since it is extremely improbable that the low-momentum Σ^- hyperons produced by absorption would travel 2.5 cm. before undergoing decay).
2. Possible scatterings or possible $\Sigma^- \pi^0 p$. These events may be subdivided according to the fate of the Σ^- hyperon.
   (a) $\Sigma^- \pi^0 p$ events (Fig. 4). For these the Σ^- hyperon

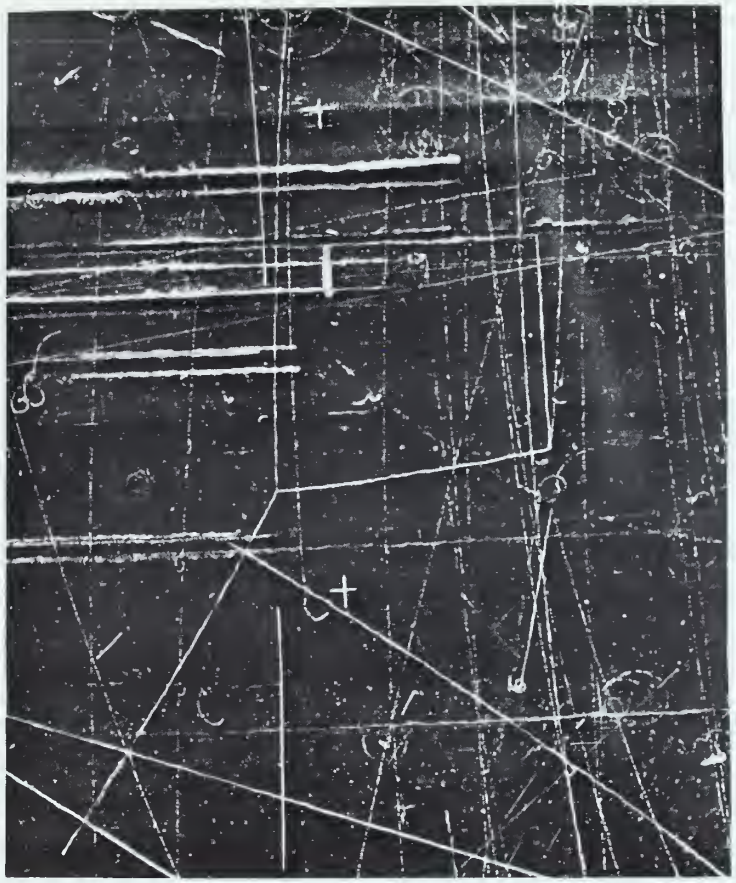

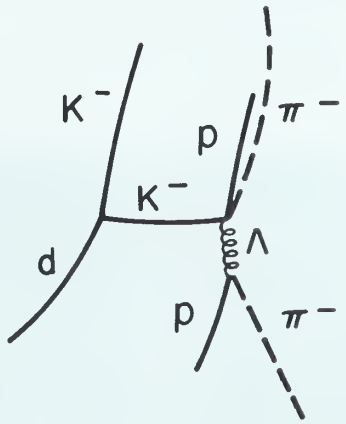

ZN-2151

Fig. 3. Definite K^- - D scatter.

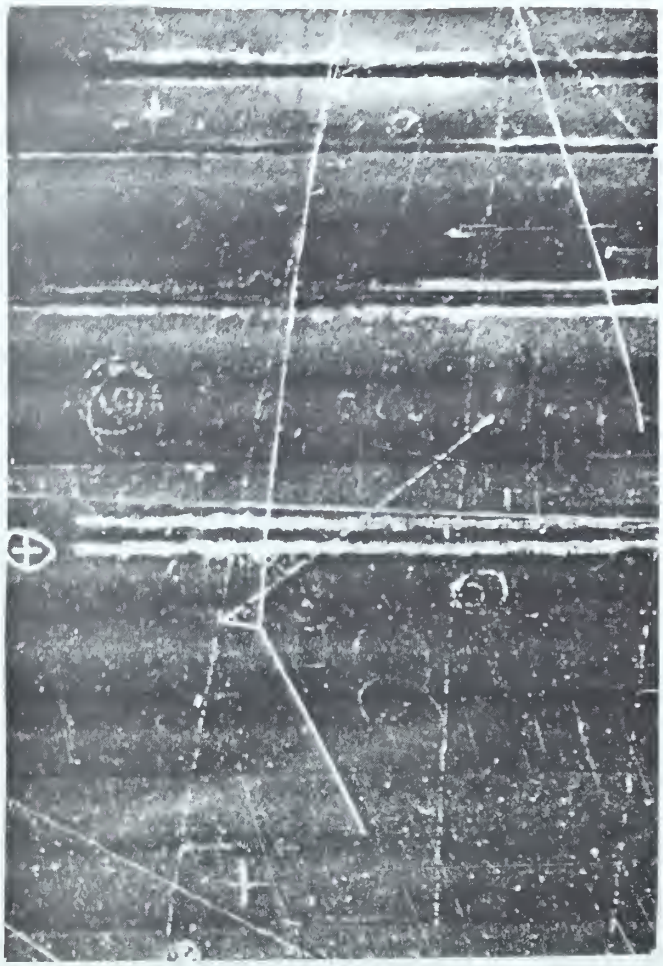

Fig. 4. Possible scatter, possible $\Sigma^- \pi^0 p$ with Σ^- decay

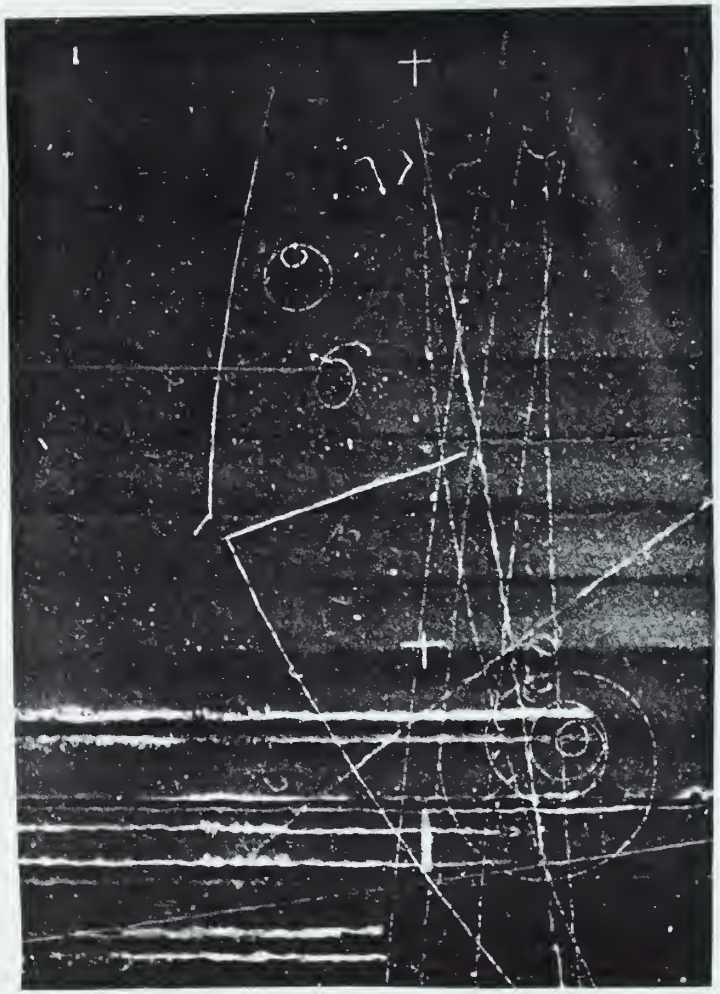

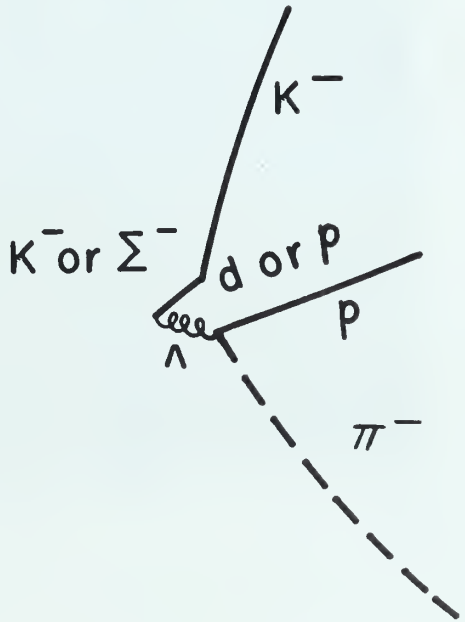

ZN-2150

Fig. 5. Possible scatter, possible $\Sigma^- \pi^0 p$ with Σ^- capture

(a) charged Λ decay

(b) neutral Λ decay.

decays in flight,

$$\Sigma^- \rightarrow \pi^- + n .$$

(b) $\Sigma^-_\Lambda \pi^0 p$ events (Fig. 5). Here the Σ^- comes to rest and gets captured by a deuteron,

$$\Sigma^- + d \rightarrow \Sigma^- + n + n$$

$$\rightarrow \Lambda + n + n ,$$

and the Λ hyperon decays via the charged mode,

$$\Lambda \rightarrow \pi^- + p .$$

(c) $\Sigma^-_\rho \pi^0 p$ events (Fig 6). These events are similar to Type (2) except that the Λ decays via its neutral mode,

$$\Lambda \rightarrow \pi^0 + n .$$

We next separated the definite scatterings into elastic and inelastic scatterings. If we examine the kinematics plot for elastic scattering, we see that it can be roughly divided into three regions of recoil-deuteron momentum (Fig. 7). For elastic scatterings in region A, the recoil deuteron is not visible in the bubble chamber because of its low momentum. On the other hand, the deuteron is always visible for elastic scatterings in region C. If the elastic scattering falls in region B, the deuteron may or may not be visible, depending on its dip angle. On the basis of a comparison between measured and computed values for both the elastic and inelastic hypotheses, each definite scattering was classified as elastic, inelastic, or indeterminate. The indeterminate scatterings were further broken down by assigning a possible and probable classification. The criteria used, in order of relative weight assigned, are:

a. momentum and (or) length of recoil deuteron,
b. angle between incident K^- and deuteron,
c. coplanarity of event,
d. momentum transfer to the deuteron,
e. momentum of incident K^-.

This classification of events is shown in Table I.

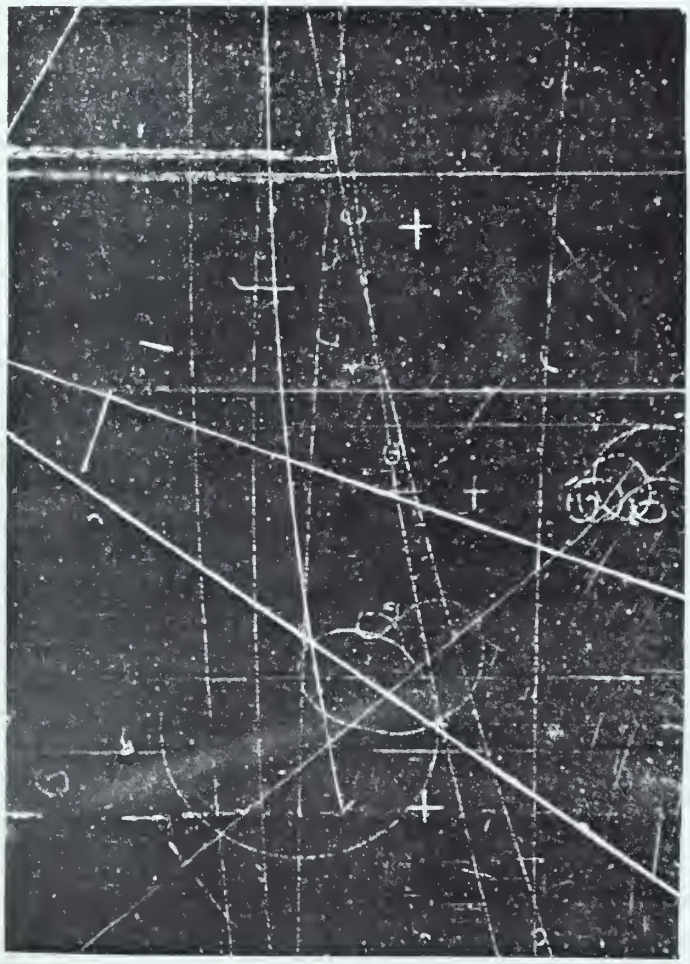

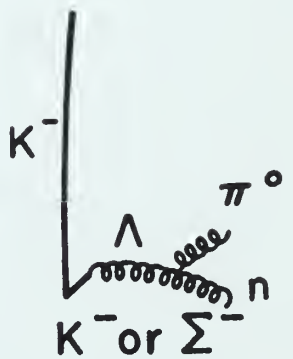

ZN-2153

Fig. 6. Elastic scatter kinematics plot.

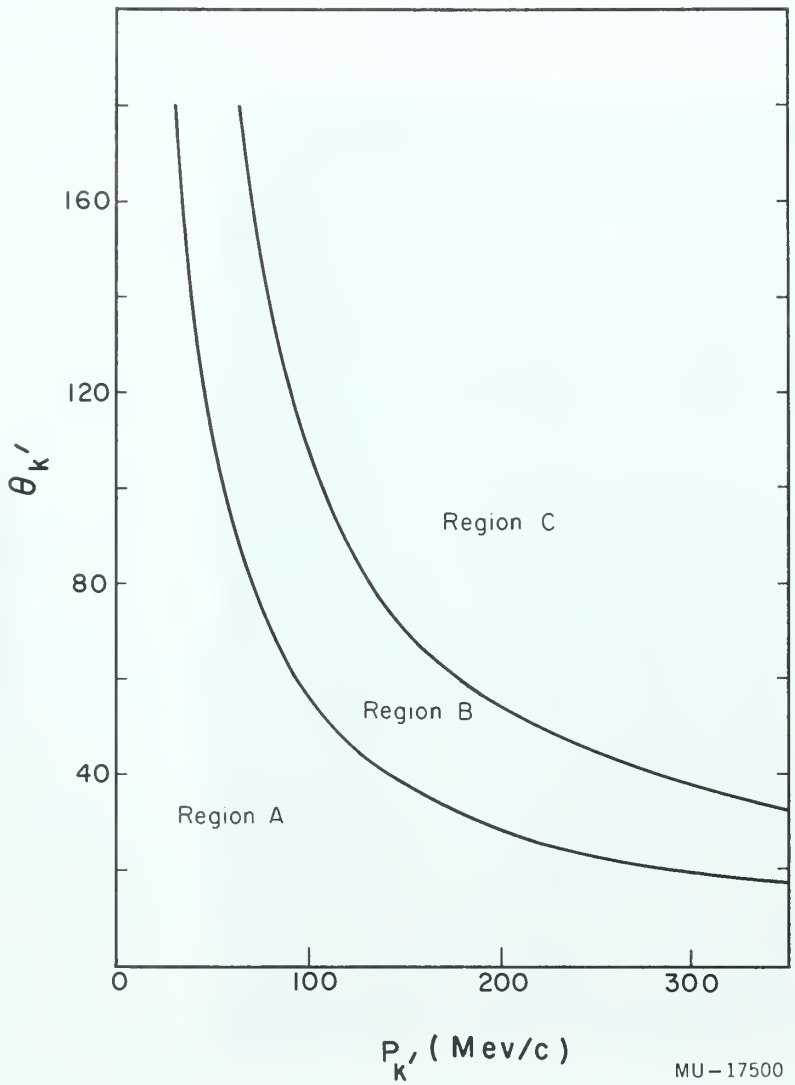

Fig. 7. Form factor vs. q .

Table I

Definite-scattering classification		
Elastic		112
Inelastic		42
Indeterminate		12
a. Probable elastic	3	
b. Probable inelastic	3	
c. Equally probable	6	
Total		176

The determination of an interaction as an elastic or inelastic scattering was essentially a subjective question of relative goodness of fit. In general, whenever an event could be fitted to the elastic-scattering kinematics within limits, it was assumed to be elastic, although it obviously always fits the inelastic kinematics better. Therefore by relaxing our fitting criteria slightly, we could combine the elastic and probable elastic scatterings in a single group. We note that this re-classification of indeterminate scatterings into elastic and inelastic scatterings is in the same ratio as the initial elastic-to-inelastic classification.

It was then necessary to estimate the number of $\Sigma^- \pi^0 p$ events in the possible scattering, possible $\Sigma^- \pi^0 p$ group. Real scatterings that contribute to this group arise from the scatterings followed by Reaction (6) or K^- decay. To estimate the contribution for Reaction (6) we may extrapolate from the number of observed scatterings followed by well-identified events. A tabulation of all scatterings according to length of the scattered track and final interaction is shown in Table II.

Table II

Event Ending	Length of scattered track L_2 2.5 c.m.	L_2 2.5 c.m.
$\Lambda\ \pi^0\ n$	23	15
$(\Lambda)\ \pi^0\ n$ [a]	10	9
K^- decay	13	40
K^- through	21	0
$\Lambda\ \pi^-p$	17	7
$(\Lambda)\ \pi^-p$	9	5
$\Sigma^-\ \pi^-p$	13	14
$\Sigma^-_\rho\ \pi^+n$	1	2
$\Sigma^-_\Lambda\ \pi^+n$	0	1
$\Sigma^+_+\ \pi^-n$	6	6
$\Sigma^+_0\ \pi^-n$	5	1
$\Sigma^\pm\ \pi^\pm n$	4	2
Scattering [b]	13	3

[a] (Λ) indicates the decay was the neutral mode

[b] event following scattering in question was a possible scattering.

We select the $\Lambda\pi^-p$, $\Sigma^+_+\pi^-n$, $\Sigma^-_-\pi^+n$, and $\Sigma^{\pm}\pi^{\mp}n$ interactions. Of the 956 events of these types observed in the fiducial volume of the chamber, 29 scattered within 2.5 c.m. of the final interaction. Therefore, for the 470 $\Lambda\pi^0n$ and $(\Lambda)\pi^0n$ interactions observed, we expect

$$\approx 470 \left(\frac{29}{956} \right) \approx 16 \pm 4$$

of these events to have scatterings within 2.5 c.m. of the interaction. This leaves 24 - 16 = 8 $\Sigma^-\pi^0p$ events in this group. From the Λ-decay branching ratio, we expect 5 $\Sigma^-_\Lambda\pi^0p$ and 3 $\Sigma^-_\rho\pi^0p$ interactions. If we make the same calculation, accepting all of the 1700 observed interactions except the $\Lambda\pi^0n$, $(\Lambda)\pi^0n$ and K^- decay events, we obtain from Table II

$$\approx 470 \left(\frac{41}{1700-470} \right) \approx 16$$

as the number of $\Lambda\pi^0n$ events with scatterings within 2.5 c.m. of the interaction.

We also expect a contribution to the possible $\Sigma^-\pi^0p$ classification from those scatterings which are followed by a K^- decay. By measurement, we find that the average path length in the fiducial volume of the chamber for a K^- meson before undergoing decay was 8.4 c.m. Since 13 K^- mesons scattered at distances greater than 2.5 c.m. from the decay vertex, we expect

$$\frac{2.5}{8.4 - 2.5} (13) \approx 5$$

actual scatters within 2.5 c.m. of the vertex. This leaves 40 - 5 = 35 real events of the Type (4). The predicted $\Sigma^-\pi^0p$ separation is shown in Table III.

Table III

Predicted $\Sigma^- \pi^0 p$ separation

	$\Sigma^- \pi^0 p$	Scatterings
Possible Σ^-	35	5
Possible Σ^-_Λ	5	10
Possible Σ^-_ρ	3	6

In addition, an independent decision was made as to classification of each possible scattering—possible $\Sigma^- \pi^0 p$ event from examination of the kinematic fit to the elastic- and inelastic-scattering hypotheses. Some of these interactions did not fit a scattering with the K^- momentum available in the incident beam and could be immediately classified as $\Sigma^- \pi^0 p$ events. In general, possible $\Sigma^- \pi^0 p$ interactions for which the incident K^- meson appeared to come to rest were classified as definite $\Sigma^- \pi^0 p$. The remaining interactions in this group were considered indeterminate and assigned a possible or probable classification as before. Table IV summarizes the experimental $\Sigma^- \pi^0 p$ separation.

Table IV

Experimental $\Sigma^- \pi^0 p$ separation		
Definite $\Sigma^-_- \pi^0 p$		29
Indeterminate		11
a. Probable $\Sigma^-_- \pi^0 p$	4	
b. Probable scatter	3	
c. Equally probable	4	
Definite $\Sigma^-_\Lambda \pi^0 p$		4
Indeterminate		11
a. Probable $\Sigma^-_\Lambda \pi^0 p$	2	
b. Probable scatter	3	
c. Equally Probable	6	
Definite $\Sigma^-_\rho \pi^0 p$		2
Indeterminate		7
a. Probable $\Sigma^-_\rho \pi^0 p$	1	
b. Probable scatter	4	
c. Equally probable	2	

Once again the fitting criteria were relaxed so that probable $\Sigma^-\pi^0 p$ became definite $\Sigma^-\pi^0 p$, and scatterings (both probable and equally probable) became definite elastic or inelastic scatterings to be separated as in the definite-scattering group. We conclude that we have 35 $\Sigma^-\pi^0 p$, 6 $\Sigma^-_\Lambda \pi^0 p$, and 3 $\Sigma^-_\rho \pi^0 p$.

Path-Length Determination

Since only the scatterings occurring in the fiducial volume were accepted for analysis, it was necessary to calculate the K^- path length in this volume for various momentum intervals so that cross sections might be computed. An IBM 650 program was devised to compute

a. the momentum of each incident K^- meson at its entrance to the fiducial volume ($P_{chamber}$),

b. its total path length in the fiducial volume.

To circumvent the problem of a possible scanning bias against observing higher--momentum K^- mesons that did not interact, only tracks entering the fiducial volume with momentum less than 225 Mev/c were retained. This is the minimum momentum for a K^- meson just passing completely through the fiducial volume without interacting. An examination of the momentum distribution at the entrance to the fiducial volume for those scatterings followed by K^- mesons undergoing decay showed two that entered with momentum less than 225 Mev/c. Since the path-length contribution to the momentum intervals is not the same for a typical K^- decay as for the other K^- interactions, it was decided that this group could be eliminated without seriously affecting our over-all statistical accuracy. This also eliminated from the data the $\Sigma^-\pi^0 p$ events.

Another IBM program was used to sum up the K^- path length in 25-Mev/c intervals for $0 \leq P_{chamber} \leq 225$ Mev/c. The $\Lambda\pi^0 n$ and $\Lambda\pi^- p$ groups were taken as typical, completely measured groups for input to this program. The summation was made first by using momentum via curvature or momentum via range, depending on which was higher. This gave a minimum path length, especially at low

momenta, because when the momentum via curvature is only slightly higher than momentum via range, the path-length contribution to intervals below 100 Mev/c is lost. Then the summation was made using momentum via range. This gave the maximum path length because it treats all tracks as stopping, and in reality there is a 20% in-flight contamination. However, it is considered that the latter determination is more nearly correct, and the accepted values were taken between the two calculated path lengths but nearer the momentum-via-range value. These were normalized to the total number of incident K^- mesons and the final path lengths are shown in Table V.

Table V

K^- path lengths	
$P_{chamber}$ interval	Path length
50 to 74 Mev/c	432 ± 102 c. m.
75 to 99	1050 ± 199
100 to 124	2025 ± 224
125 to 149	3205 ± 159
150 to 174	4305 ± 49
175 to 199	4310 ± 116
200 to 224	2260 ± 80

THEORETICAL CONSIDERATIONS

For elastic scattering from a single particle at the origin, the wave function at any point is[4]

$$\psi(\vec{r}) = \exp(i\vec{K} \cdot \vec{r}) + f(\theta, \phi) \frac{\exp(iKr)}{r},$$

where the first term is the incident wave and the second term is the scattered wave. All quantities are evaluated in the center-of-mass coordinate system. If we consider only S-wave scattering, the scattering amplitude is

$$f(\theta, \phi) = T \text{ (a constant)}.$$

If the scattering center is not at the origin, the scattered wave is given by

$$T \frac{\exp(iK \left| \vec{r} - \vec{r}_0 \right|)}{\vec{r} - \vec{r}_0} \exp(i\vec{K} \cdot \vec{r}_0)$$

where $\vec{r}_0$ is the location of the scattering center and $\exp(i\vec{K} \cdot \vec{r}_0)$ represents the amplitude of the incident wave at the scattering center. When considering elastic scattering from the deuteron (i. e., the deuteron does not break up during the collision) we may obtain a first approximation to the proton-scattered amplitude by averaging over the location of the scattering center of the deuteron, as shown in Fig. 8.

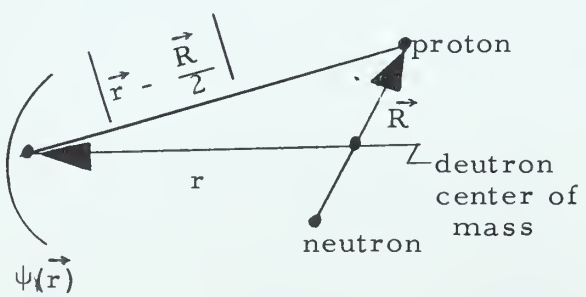

Fig. 8. Geometry of scattering.

In this approximation, the total scattered wave from the proton (located at $\frac{\vec{R}}{2}$) is

$$T_p \int \exp(i\vec{K}\cdot\vec{r}_0)\frac{\exp\left(iK\left|\vec{r}-\frac{\vec{R}}{2}\right|\right)}{\left|\vec{r}-\frac{\vec{R}}{2}\right|}\left|\psi_D(R)\right|^2 dV_R \ .$$

Now we see

$$\left|\vec{r}-\frac{\vec{R}}{2}\right| = \left(r^2 - \vec{r}\cdot\frac{\vec{R}}{2} + \frac{R^2}{4}\right)^{\frac{1}{2}}$$

$$\approx r\left[1 - \frac{\vec{r}\cdot\vec{R}}{2r^2}\right]$$

$$\approx r - \frac{\vec{r}\cdot\vec{R}}{2r} \ ,$$

so that the scattered wave becomes

$$T_p \int \exp(i\vec{K}\cdot\vec{r}_0)\ \frac{\exp\left(iK\left[r - \frac{\vec{r}\cdot\vec{R}}{2r}\right]\right)}{r}\left|\psi_D(R)\right|^2 dV_R \ ,$$

where $\frac{\vec{r}\cdot\vec{R}}{2r}$ is small enough to be ignored in the denominator but not in the exponential, where it acts like a phase shift. Since we have $\vec{r}_0 = \frac{\vec{R}}{2}$ we have also

$$T_p \frac{\exp(iKr)}{r}\int \exp\left(i\vec{K}\cdot\frac{\vec{R}}{2}\right)\exp\left(-i\vec{K}'\cdot\frac{\vec{R}}{2}\right)\left|\psi_D(R)\right|^2 dV_R$$

$$= T_p \frac{\exp(iKr)}{r}\int \exp\left(i\vec{q}\cdot\frac{\vec{R}}{2}\right)\left|\psi_D(R)\right|^2 dV_R$$

where $\vec{q} = \vec{k} - \vec{k}'$ and $\vec{k}$ is the incident K^- momentum in the K^--d center-of-mass system and $\vec{k}'$ is the outgoing K^- momentum in the same coordinate system. By the same argument, the scattered wave from the neutron is

$$T_n \frac{\exp(iKr)}{r} \int \exp\left(i\vec{q} \cdot \frac{\vec{R}}{2}\right) \left|\psi_D(R)\right|^2 dV_R$$

and the total scattered wave is

$$(T_n + T_p) \frac{\exp(iKr)}{r} \int \exp\left(i\vec{q} \cdot \frac{\vec{R}}{2}\right) \left|\psi_D(R)\right|^2 dV_R .$$

The integral becomes

$$F(q) = \int \exp\left(iq \frac{R}{2} \cos\theta\right) \left|\psi_D(R)\right|^2 R^2 \, dR \, d\Omega$$

$$= 2\pi \int \exp\left(iq \frac{R}{2} \cos\theta\right) \left|\psi_D(R)\right|^2 R^2 \, dR \, d(\cos\theta)$$

and we see that we have

$$\int \exp\left(iq \frac{R}{2} \cos\theta\right) d(\cos\theta) = \frac{\exp\left(iq \frac{R}{2} \cos\theta\right)}{iq \frac{R}{2}} \Bigg|_{\cos\theta=-1}^{\cos\theta=1}$$

$$= \frac{\exp\left(iq' \frac{R}{2}\right) - \exp\left(-iq \frac{R}{2}\right)}{iq \frac{R}{2}} = \frac{2 \sin\left(q \frac{R}{2}\right)}{q \frac{R}{2}}$$

Thus the scattered amplitude is

$$\psi_{scat} = (T_n + T_p) \frac{\exp(iKr)}{r} \int \frac{4\pi \sin\left(q \frac{R}{2}\right)}{q \frac{R}{2}} \left|\psi_D(R)\right|^2 R^2 \, dR.$$

In general,

$$\frac{d\sigma}{d\Omega} = r^2 \psi^*_{scat} \psi_{scat} = \left|T_n + T_p\right|^2 \left|\frac{F(q)}{F(0)}\right|^2 .$$

It is now necessary to evaluate the elementary scattering amplitudes in the K^--nucleon system in terms of experimentally determined phase shifts. For S-wave scattering we have

$$\psi_{total} = \text{const} \ \frac{\sin (Kr + \delta)}{Kr}$$

$$= \text{const} \ \frac{\sin Kr \cos \delta + \cos Kr \sin \delta}{Kr},$$

where δ is the S-wave phase shift. But in general we had

$$\psi = \exp (iK \cdot r) + T \frac{\exp (iKr)}{r} \ ,$$

and if we now break this up into angular-momentum states and take only the S-wave ($\ell = 0$) part, we obtain

$$\exp (i\vec{K} \cdot \vec{r}) = \sum_{\ell} (2\ell + 1) \, i^{\ell} j_{\ell}(Kr) \, p_{\ell}(\cos \theta)$$

$$\approx \frac{\sin Kr}{Kr} \ .$$

Therefore

$$\psi = \frac{\sin Kr}{Kr} + KT \ \frac{\cos Kr + i \sin Kr}{Kr}$$

$$= \frac{1 + iKT}{Kr} \ \sin Kr + \frac{KT \cos Kr}{Kr}$$

$$= \left[\frac{1 + i \, KT}{Kr}\right] \left[\sin Kr + \left(\frac{1}{1 + i \, KT}\right) (KT \ \cos \ Kr)\right] .$$

But we also had

$$\psi = \text{const} \ \frac{\cos \delta}{Kr} \ \left[\sin Kr + \tan \delta \cos Kr\right] .$$

Identifying terms, we get

$$\tan \delta = \frac{KT}{1 + i\, KT}$$

$$\tan \delta + i\ KT \tan \delta = KT$$

$$T = \frac{\tan \delta}{K(1 - i\ \tan \delta)};$$

also

$$(1 + i\, KT) \tan \delta = KT,$$
$$(1 + i\, KT) \sin \delta = KT \cos \delta,$$
$$(1 + i\, KT) \left[\exp(i\delta) - \exp(-i\delta)\right] = iKT \left[\exp(i\delta) + \exp(-i\delta)\right]$$
$$(1 + i\, KT) \left[\exp(2i\delta) - 1\right] = iKT \left[\exp(2i\delta) + 1\right]$$
$$\exp(2i\delta) - (1 + iKT) = iKT$$
$$2\, iKT = \exp(2i\delta) - 1$$
$$T = \frac{\exp(2i\delta) - 1}{2iK}$$

This then is the formula for the scattering amplitude, T, in terms of of the S-wave phase shift, δ.

Actually the K^--p system is a combination of equal parts of the two isotopic spin states, I = 0 and I = 1,

$$K^-_p = \frac{1}{\sqrt{2}} \left[\chi\ (1) + \chi\ (0)\right].$$

In the zero-effective-range approximation, the phase shifts are related to the S-wave scattering lengths, A_0 and A_1, by the formulas

$$\tan \delta_0 = K\, A_0,$$
$$\tan \delta_1 = K\, A_1,$$

where A_0 and A_1 are complex because of the absorptive processes (hyperon production, etc.) that can occur. From the experimental K^--p data, Daltiz has computed two possible solutions for the scattering lengths as shown in Table VI.[5]

Table VI

	$A_0 (\times 10^{13}$ cm)	$A_1 (\times 10^{13}$ cm)
Soln a	± 0.20 + 0.76i	± 1.62 + 0.38i
Soln b	± 1.88 + 0.82i	± 0.40 + 0.41i

The real parts of both solutions have the same relative sign but the absolute sign is not determined.

In the K^--neutron system, only the I = 1 state is involved, thus

$$K^- N = \chi \ (1) \ .$$

When we relate the scattering lengths to the scattering amplitudes through

$$T_I = \frac{A_I}{1 + i \, K A_I} \ ,$$

we can find the scattering amplitudes for deuterium. Since we have

$$T_p = \frac{T_1 + T_0}{T_1^{\,2}} \ ,$$

we can write

$$T_n + T_p = \frac{3}{2} \ T_1 + \frac{1}{2} \ T_0 \ .$$

RESULTS

Using the ideas presented in the preceding section, Gourdin and Martin have calculated the theoretical differential cross section for elastic scattering in deuterium.[6] In the laboratory system it is

$$\frac{d\sigma}{d(\cos\theta)} = 2\pi \left| T_n + T_p \right|^2 \left| \frac{F(q)}{F(0)} \right|^2 \frac{d(\cos\theta_{c.m.})}{d(\cos\theta)} .$$

They have evaluated the effects of the form factor, $\left| \frac{F(q)}{F(0)} \right|^2$, using the equation

$$F(q) = \frac{2}{qr} \int_0^\infty \left| \psi_D(r) \right|^2 \sin \frac{qr}{2} \, r^2 \, dr .$$

Assuming that the deuteron is adequately described by the Hulthen wave function, we have

$$\psi_D(r) = \frac{1}{r} \left[\exp(-\beta r) - \exp(-\alpha r) \right].$$

Gourdin and Martin find

$$\frac{F(q)}{F(0)} = \frac{1}{q} \frac{4\alpha\beta(\alpha+\beta)}{(\beta-\alpha)^2} \tan^{-1} \frac{16\, q\, (\beta-\alpha)^2(\beta+\alpha)}{q^4+4q^2\left[(\beta-\alpha)^2+2(\beta+\alpha)^2\right]+64\alpha\beta(\alpha+\beta)^2},$$

where $\alpha = 45.7$ and $\beta = 7\alpha$. A plot of $\left| \frac{F(q)}{F(0)} \right|^2$ vs q is presented in Fig. 9. This general curve can be used to obtain the differential cross section at particular laboratory-system momenta. For 175 Mev/c (lab) we have computed $\left| T_n + T_p \right|^2$. For the two Dalitz solutions we find

Solution a: $\left| T_n + T_p \right|^2 = 3.45,$

Solution b: $\left| T_n + T_p \right|^2 = 2.95 .$

The resulting differential cross section for elastic scattering is shown in Fig. 10.

To obtain the total elastic cross section we have evaluated the integrals,

$$\sigma = \int \frac{d\sigma}{d\Omega} d\Omega = 2\pi \int \frac{d\sigma}{d\Omega} \quad d\cos\theta$$

$$= 2\pi \int \left|\frac{F(q)}{F(0)}\right|^2 \left|T_n + T_p\right|^2 d\cos\theta \ .$$

Simpson's rule was used to obtain $\int \left|\frac{F(q)}{F(0)}\right|^2 \quad d\cos\theta$ from Fig. 11 for several values of incident K^--meson laboratory-system momenta, and total elastic cross sections were computed.

A plot of the angular distribution of the experimentally determined scatterings shows a large peak in the forward direction. This indicates that the Coulomb scattering effect is large, and since it is not easily calculable, we have discarded all scatterings with $\cos\theta \geq 0.95$ (lab) and have corrected the total cross sections for this effect.

In an analogous manner, using the equations of Gourdin and Martin, we have computed the differential and total inelastic cross sections.

Because of statistical limitations in our data, we have used path lengths to predict the number of events we should expect to see in each momentum interval for Solution a or for Solution b. Thus we have

$$N = \ell\ \sigma\ N_0 = \ell\ \sigma\ (.0642)\ (6.03 \times 10^{23})\ (10^{-27})$$

$$= (3.85 \times 10^{-5})\ \ell\ \sigma \ ,$$

where σ is in millibarns. A summary of the predicted values is shown in Table VII.

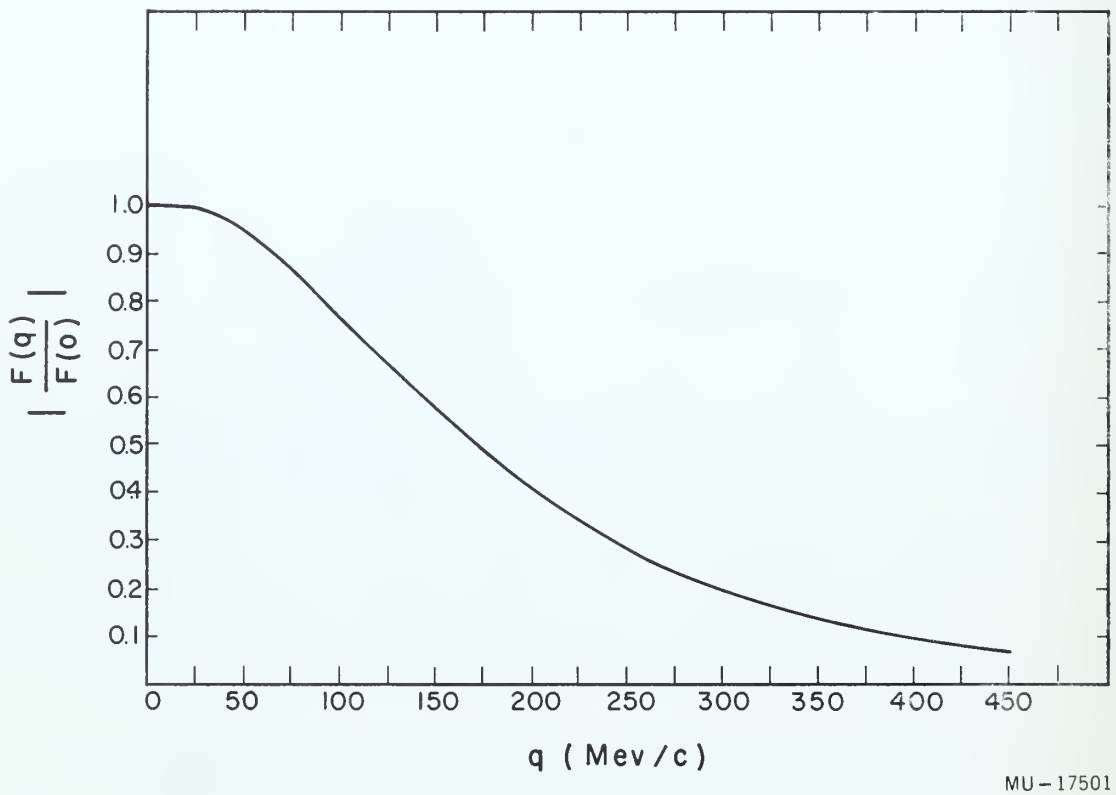

Fig. 9. Form factor vs cos $\theta_{c.m.}$.

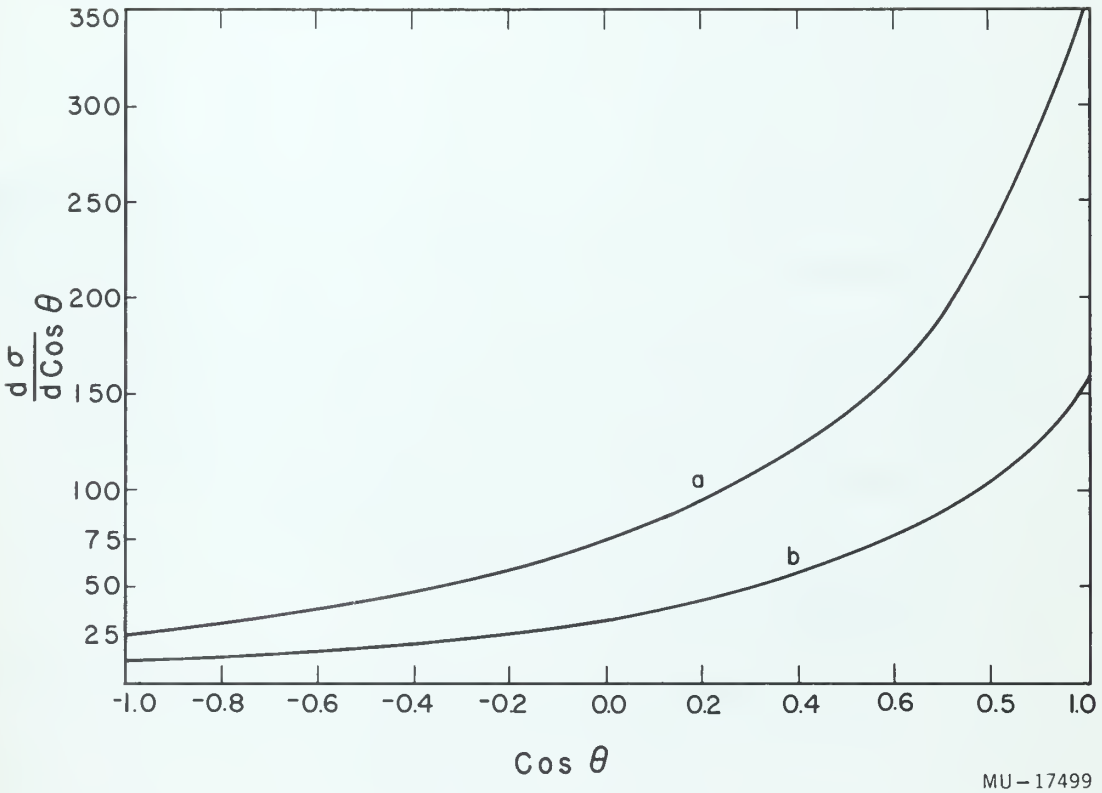

Fig. 10. Total scattering cross-sections - Solution a.

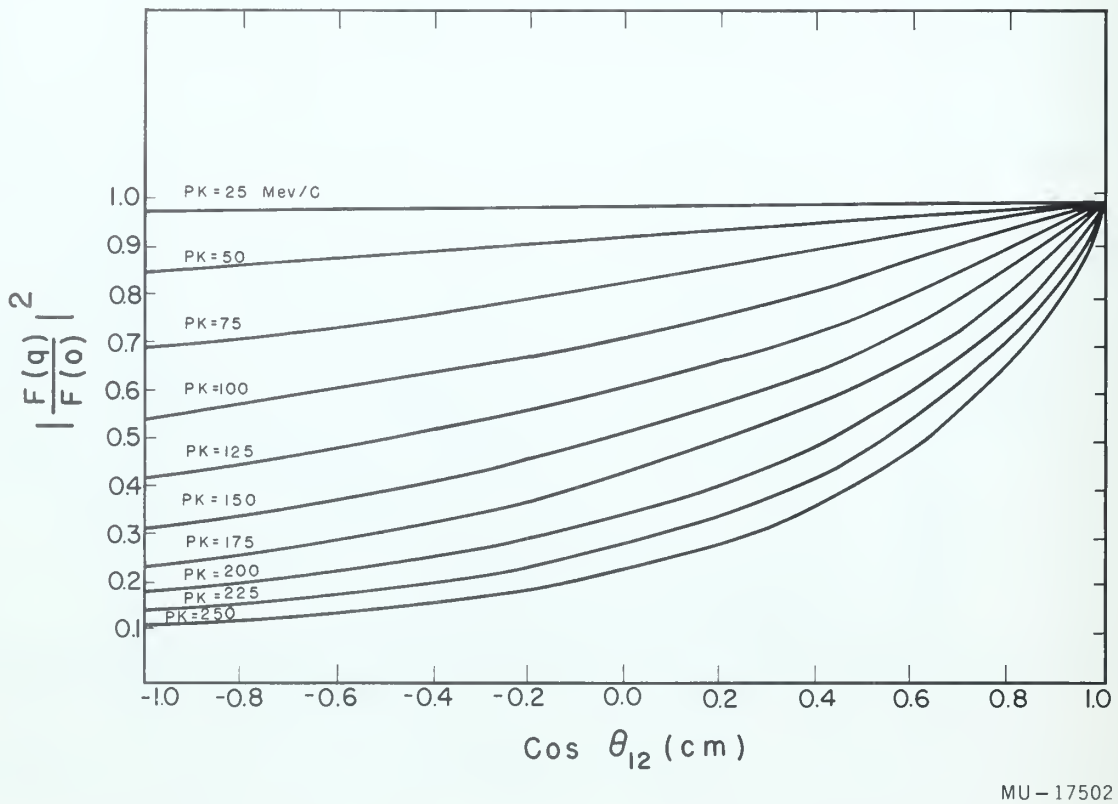

Fig. 11. Total scattering cross-sections - Solution b.

Table VII

Predicted cross-section data										
P_{lab} interval (Mev/c)	σ_{el} (mb)		σ_{inel} (mb)		σ_t (mb)		Corrected σ_t (mb)		N_t	
	a	b	a	b	a	b	a	b	a	b
100 - 149	359	150	74	38	433	188	406	179	86	38
150 - 199	210	92	73	39	281	130	262	120	91	42
200 - 224	139	64	64	35	202	99	187	87	17	8
									194	88

We can compare the experimentally determined number of scatterings and the predicted numbers to determine which solution is correct. If we accomplish this through the total scattering cross section, our elastic- and inelastic-scattering separation is not involved. We find 58 scatterings occurring between 100 and 225 Mev/c that fit our acceptance criteria, and therefore conclude that Solution b is correct.

In summary, we present the elastic, inelastic, and total scattering cross sections for the two solutions in Figs. 12 and 13. We have also plotted the experimentally determined cross sections for P_{lab} = 125, 175, and 212.5 Mev/c. In Fig. 14 we have normalized the theoretical curves to the observed numbers of events in order to compare the shapes of the angular distributions.

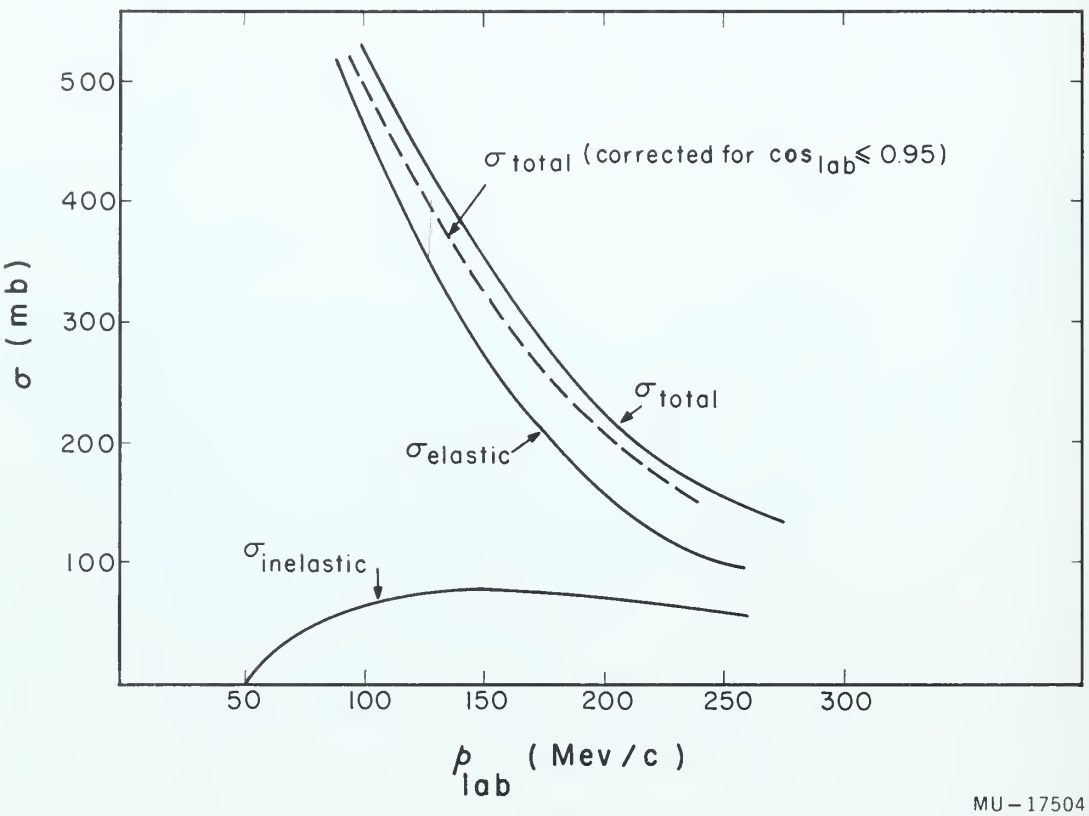

Fig. 12. Normalized angular distribution at 175 Mev/c.

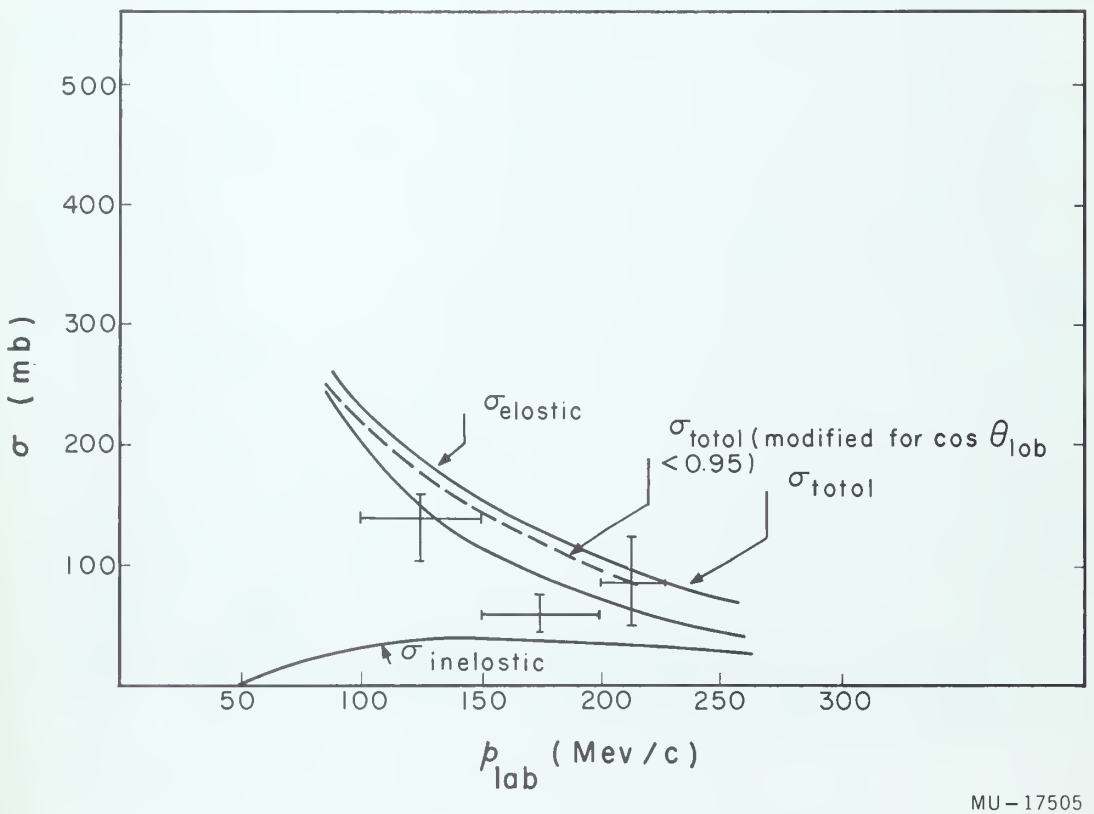

Fig. 13. Total scattering cross-sections, solution 6.

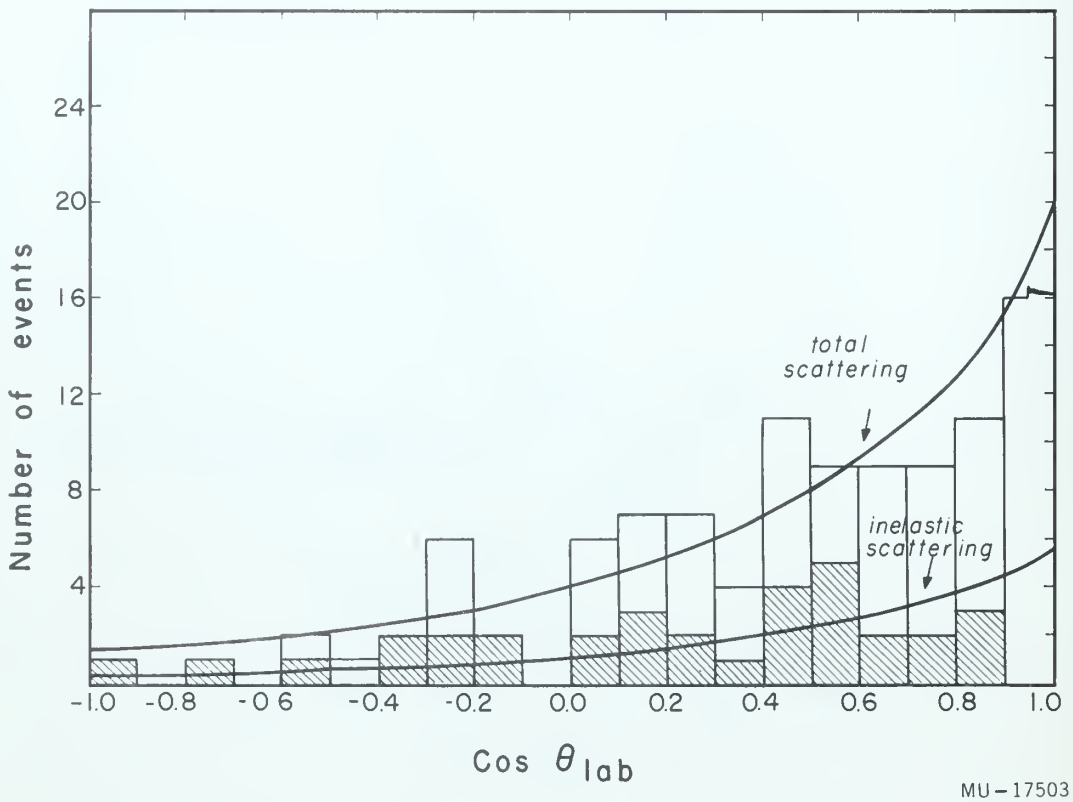

Fig. 14. Normalized angular distribution at 175 Mev/c
inelastic
total

CONCLUSIONS

Because of the enormous difference in the predicted K^--D cross sections for the two Dalitz phase-shift solutions, it has been possible to make a strong argument for Solution b, even with the limited statistical data available. It must be remembered that this conclusion is independent of our ability to separate elastic and inelastic scatterings, since only the total cross sections were used.

In addition, comparison of the elastic and inelastic components of the scattering events with the theoretical curves shows that the simple model used by Gourdin and Martin to calculate the scattering in deuterium is adequate to describe the angular distributions, and, approximately, the ratio of inelastic to elastic events. It will be noticed however, that the absolute values measured are consistently lower than those predicted. It is expected that more detailed theoretical calculations which include the effects of secondary scattering will result in lower cross sections than presented here. If future calculations show that the scattering amplitude for Solution b can be depressed by 50%, then the predicted cross sections will decrease by 100% and no conclusion can be drawn from this experiment. Experience with the effects of higher-order (multiple-scattering) effects in the π-meson nuclear system leads one to expect that such a large depression will not occur.

ACKNOWLEDGMENTS

I wish to express my appreciation to Dr. Luis W. Alvarez, head of the Bubble Chamber Group at Lawrence Radiation Laboratory, for making this investigation possible; to Dr. Donald H. Miller, for devoting an enormous amount of time and effort to directing this research and the writing of this paper; to J. Peter Berge, Orin Dahl, Louise Holstein, and Joseph Schwartz for compiling the IBM 650 programs required, and, finally, to the entire bubble chamber film-scanning group.

This work was done under the auspices of the U. S. Atomic Energy Commission.

APPENDIX

A. Elastic Scattering Analysis for $K^- + d \rightarrow K^- + d$

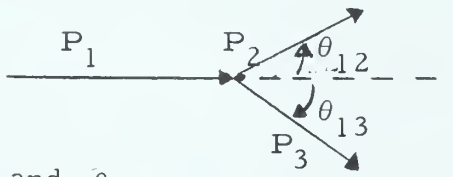

1 $\triangleq$ incident K′
2 $\triangleq$ scatter K′
3 $\triangleq$ recoil d

Given: $\vec{P}_2$ and θ_{12}
Find: $\vec{P}_1$, $\vec{P}_3$, θ_{13}, θ_{12}(c.m.), $L^c{}_3$ (proj)

Let $\vec{P}_1$ be in the x direction and the plane of $\vec{P}_2$ and $\vec{P}_3$ be the xy plane. From momentum and energy conservation we get

$$P_1 = P_2 \cos\theta_{12} + P_3 \cos\theta_{13}, \tag{A1}$$

$$0 = P_2 \sin\theta_{12} + P_3 \sin\theta_{13}, \tag{A2}$$

$$\frac{P_1^2}{2m_K} = \frac{P_2^2}{2m_K} + \frac{P_3^2}{2m_d}. \tag{A3}$$

Solving (A1) and (A2) for P_3

$$P_3^2 = P_1^2 - 2P_1P_2\cos\theta_{12} + P_2^2 \tag{A4}$$

Multiplying (A3) by $2m_K$

$$P_1^2 = P_2^2 + \frac{m_K}{m_d} P_3^2 = P_2^2 + R P_3^2 \tag{A5}$$

Substituting (A4) in (A5) and dividing by P_2^2, we get the quadratic eqn.

$$(1-R)\left(\frac{P_1}{P_2}\right)^2 + 2R\cos\theta_{12}\frac{P_1}{P_2} - (1+R) = 0 \tag{A6}$$

with the solution

$$\frac{P_1}{P_2} = \frac{1}{1-R}\left[-R\cos\theta_{12} + \sqrt{R^2\cos^2\theta_{12} + (1-R^2)}\right] \tag{A7}$$

Dividing (A5) by P_2^2 we get

$$\frac{P_3}{P_2} = \sqrt{\frac{1}{R}\left[\left(\frac{P_1}{P_2}\right)^2 - 1\right]} \tag{A8}$$

From (A2)

$$\sin \theta_{13} = \frac{P_2}{P_3} \quad \sin \theta_{12} = \frac{\sin \theta_{12}}{P_{3/P_2}} \tag{A9}$$

In the center-of-mass system

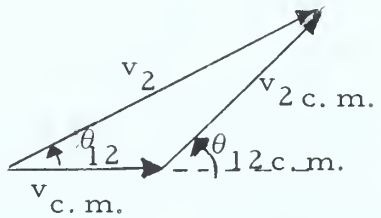

$$\tan \theta_{12c.m} = \frac{v_2 \sin \theta_{12}}{v_2 \cos \theta_{12} - v_{c.m.}} = \frac{\sin \theta_{12}}{\cos \theta_{12} - \frac{v_{c.m.}}{v_2}}$$

$$\frac{v_{c.m.}}{v_2} = \frac{m_K}{m_d + m_K} \frac{v_1}{v_2} = \frac{P_1/P_2}{\frac{m_d + m_K}{m_K}} = \frac{P_1/P_2}{1 + 1/R}$$

Therefore

$$\tan \theta_{12\,c.m.} = \frac{\sin \theta_{12}}{\cos \theta_{12} - \frac{P_1/P_2}{1 + 1/R}} \tag{A10}$$

Now

$$L_3(\text{proj}) = L_3 \cos \lambda_3 = L_3 \cos \left(\frac{\pi}{2} - \cos^{-1} \gamma_3 \right)$$

We find γ_3 by using unit vectors and the three equations

$$\hat{n}_1 \times \hat{n}_2 = \hat{p} \sin \theta_{12}\,, \tag{A11}$$

$$\hat{n}_3 \times \hat{n}_1 = \hat{p} \sin \theta_{13}, \tag{A12}$$

$$\hat{n}_3 \times \hat{n}_2 = \hat{p} \sin \theta_{23}\,. \tag{A13}$$

Solving for p and taking the j components, we obtain

$$\frac{1}{\cos \theta_{12}} (\gamma_1 \alpha_2 - \gamma_2 \alpha_1) = \frac{1}{\cos \theta_{13}} (\gamma_3 \alpha_1 - \gamma_1 \alpha_3) = \frac{1}{\cos \theta_{23}} (\gamma_3 \alpha_2 - \gamma_2 \alpha_3)\,.$$

Using any of various combinations of the two equalities, we solve for

$$\gamma_3 = \frac{\gamma_1 \sin \theta_{23} - \gamma_2 \sin \theta_{13}}{\sin \theta_{12}}\,. \tag{A14}$$

B. Inelastic-Scattering Analysis for $K^- + d \rightarrow K^- + p + n$

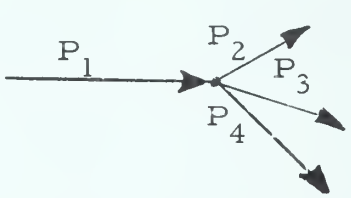

$1 \triangleq$ incident K^-
$2 \triangleq$ scatter K^-
$3 \triangleq$ recoil P
$4 \triangleq$ recoil n

Given: P_2, P_3, direction cosines of $\hat{n}_1$, $\hat{n}_2$, $\hat{n}_3$.

Find: P_1, P_4, direction cosines of $\hat{n}_4$.

We let $\vec{P}_1 = P_{x_1}\,\hat{i}$ and therefore $P_{y_1} = P_{z_1} = 0$.

From momentum and energy conservation we get the equations

$$P_{x_1} = P_{x_2} + P_{x_3} + P_{x_4} , \tag{A15}$$

$$0 = P_{y_2} + P_{y_3} + P_{y_4} , \tag{A16}$$

$$0 = P_{z_2} + P_{z_3} + P_{z_4} , \tag{A17}$$

$$\frac{P_1^2}{2m_K} = \frac{P_2^2}{2m_K} + \frac{P_3^2}{2m_p} + \frac{P_4^2}{2m_n} + Q, \tag{A18}$$

where $Q = m_p + m_n - m_d = 2.229$.

We immediately can get P_{y_4} and P_{z_4} from Eqs. (A16) and (A17).

We define

$$K_1 \triangleq \frac{P_2^2}{m_K} + \frac{P_3^2}{m_p} + \frac{P_{y_4}^2 + P_{z_4}^2}{m_n} + 2Q$$

$$K_2 \triangleq P_{x_2} + P_{x_3}$$

Then, from Eqs. (A15) and (A16),

$$P_1 = K_2 + P_{x_4} , \tag{A19}$$

$$\frac{P_1^2}{m_K} = K_1 + \frac{P_{x_4}^2}{m_n} . \tag{A20}$$

Squaring Eq. (A19), substituting in Eq. (A20), and solving the resulting quadratic we get

$$P_{x_4} = -\frac{\sqrt{K_2 + K_2^2 - (1 - \frac{m_K}{m_n})(K_2^2 - m_K K_1)}}{(1 - \frac{m_K}{m_n})} \quad . \quad \text{(A21)}$$

Substituting Eq. (A21) in Eq. (A19) we solve for

$$P_1 = -\frac{\frac{m_K}{m_n} K_2 + \sqrt{\frac{m_K}{m_n} K_2^2 + (1 - \frac{m_K}{m_n}) m_K K_1}}{1 - \frac{m_K}{m_n}} \quad \text{(A22)}$$

We want a coordinate system in which $\hat{n}_1$ is in the x direction and $\hat{n}_2$ has a dip angle equal to zero. To get $\hat{n}_1$ along the x axis we make 2 successive transformations. We rotate about the z axis through an angle θ and then about the y axis through an angle $(\frac{\pi}{2} - \phi)$:

$$\begin{pmatrix} n_x' \\ n_y' \\ n_z' \end{pmatrix} = \begin{pmatrix} \sin\phi & 0 & \cos\phi \\ 0 & 1 & 0 \\ -\cos\phi & 0 & \sin\phi \end{pmatrix} \begin{pmatrix} \cos\theta & \sin\theta & 0 \\ -\sin\theta & \cos\theta & 0 \\ 0 & 0 & 1 \end{pmatrix} \begin{pmatrix} n_x \\ n_y \\ n_z \end{pmatrix}$$

The given variables are

$$n_{x_1} = \alpha, \quad n_{y_1} = \beta, \quad n_{z_1} = \gamma,$$

$$\cos\phi = \gamma,$$

$$\sin\phi = \sqrt{1 - \gamma^2},$$

$$\cos\theta = \frac{\alpha}{\sqrt{1 - \gamma^2}},$$

$$\sin\theta = \frac{\beta}{\sqrt{1 - \gamma^2}}.$$

To get $\lambda_2 = 0$ we rotate about the x axis through an angle ξ:

$$\begin{pmatrix} n_x'' \\ n_y'' \\ n_z'' \end{pmatrix} = \begin{pmatrix} 1 & 0 & 0 \\ 0 & \cos\xi & \sin\xi \\ 0 & -\sin\xi & \cos\xi \end{pmatrix},$$

where

$$\cos\varsigma = \frac{n_{y_2}'}{\sqrt{1-n_{x_2}'^2}} \triangleq a ,$$

$$\sin\xi = \frac{n_{z_2}'}{\sqrt{1-n_{x_2}'^2}} \triangleq b .$$

We get

$$n_x' = \alpha n_x + \beta n_y + \gamma n_z ,$$

$$n_y' = -\frac{\beta}{\sqrt{1-\gamma^2}} n_x + \frac{\alpha}{\sqrt{1-\gamma^2}} n_y ,$$

$$n_z' = -\frac{\alpha\gamma}{\sqrt{1-\gamma^2}} n_x - \frac{\beta\gamma}{\sqrt{1-\gamma^2}} n_y + \sqrt{1-\gamma^2}\, n_z .$$

Let

$$n_{x_2} = \delta, \quad n_{y_2} = \epsilon, \quad n_{z_2} = \rho ;$$

then

$$n_{x_2}' = \alpha\delta + \beta\epsilon + \gamma\rho,$$

$$n_{y_2}' = -\frac{\beta\delta + \alpha\epsilon}{\sqrt{1-\gamma^2}}$$

$$n_{z_2}' = -\frac{\alpha\gamma\delta - \beta\gamma\epsilon + (1-\gamma^2)\rho}{\sqrt{1-\gamma^2}}$$

and

$$n_x'' = \alpha n_x + \beta n_y + \alpha n_z \ ,$$

$$n_y'' = -\frac{(A\beta + B\alpha\gamma)n_x + (A\alpha - B\beta\alpha)n_y}{1 - \gamma^2} + Bn_z \ ,$$

$$n_z'' = \frac{(B\beta - A\alpha\gamma)n_x - (B\alpha + A\beta\gamma)n_y}{1 - \gamma^2} + An_z \ ,$$

where

$$A \triangleq a\sqrt{1 - \gamma^2} \ ,$$

$$B \triangleq b\sqrt{1 - \gamma^2} \ ,$$

$$a = \frac{\alpha\epsilon - \beta\delta}{\sqrt{1 - \gamma^2}\sqrt{1 - n_{x_2}^2}} \ ,$$

$$b = -\frac{\alpha\gamma\delta - \beta\gamma\epsilon + (1 - \gamma^2)\rho}{\sqrt{1 - \gamma^2}\sqrt{1 - n_{x_2}'^2}} \ .$$

Now we can solve for $\hat{n}_2''$, and $\hat{n}_3''$ and then for $\hat{n}_4''$. We use the reverse transformation to get $\hat{n}_4$.

C. Momentum Transfer

In the center-of-mass sytem,

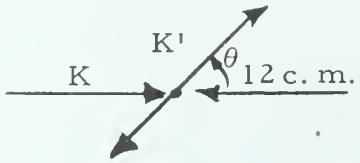

the momentum transfer is

$$\left|\vec{q}\right| = \left|\vec{K} - \vec{K'}\right| .$$

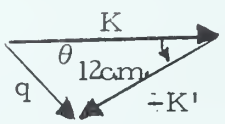

By law of cosines, we have

$$q^2 = K^2 + K'^2 - 2\,K\,K'\cos\theta_{12\,c.m.}$$

For an elastic scattering we have

$$K = K' = \frac{m_d}{m_d + m_K} P_K = 0.792\, P_K .$$

Therefore we obtain

$$q^2 = 2\,K^2 (1 - \cos\theta_{12\,c.m.})$$

$$q = \sqrt{2}\,K\sqrt{1 - \cos\theta_{12\,c.m.}}$$

$$= 1.12\, P_K \sqrt{1 - \cos\theta_{12\,c.m.}} .$$

REFERENCES

1. Murray Gell-Mann and Arthur H. Rosenfeld, Hyperons and Heavy Mesons: Systematics and Decay UCRL-3799, July 1957.
2. R. H. Dalitz, Theoretical Interpretation of Strange-Particle Interactions, UCRL-8394, Aug. 1958.
3. N. Horwitz, J. J. Murray, R. R. Ross and R. D. Tripp, 450-Mev/c K^- and $\bar{p}$ Beams at the Northwest Target Area of the Bevatron Separated by the Coaxial Velocity Spectrometer, UCRL-8269, June 1958.
4. J. M. Blatt and V. F. Weisskopf, Theoretical Nuclear Physics (John Wiley and Sons, New York, 1952).
5. R. H. Dalitz and S. F. Tuan, The Energy Dependence of Low-Energy K-Proton Processes, EFINS-59-17, March 1959.
6. M. Gourdin and A. Martin, K^--Deuterium Scattering, Laboratoire de Physique, Ecole Normale Superieure, Paris (to be published).